



Effects of substrate annealing on wettability and intermetallic compound formation in Sn–3.0Cu/Cu systems

Niwat Mookam¹ · Kannachai Kanlayasiri¹

Received: 31 January 2019 / Accepted: 22 May 2019 / Published online: 29 May 2019
© Springer Science+Business Media, LLC, part of Springer Nature 2019

Abstract

This paper investigates the effects of Cu substrate annealing on the wettability of Sn–3.0Cu lead-free solder and the subsequent growth of the intermetallic compounds that are formed at the interface between the solder and the substrate. The annealing processes yielded various grain sizes, grain orientations, and residual strains within the substrates. Then, effects of the Cu substrates on the wetting and intermetallic formation were studied via reflow soldering using Sn–3.0Cu lead-free solder. The annealed substrates were compared to an unannealed Cu reference at soldering times of 20, 40, 60 and 120 s. The experimental results demonstrated that the substrate grain orientation, residual strain and grain size exert no influence on the solder wettability. After soldering, only a η -Cu₆Sn₅ intermetallic compound was observed in the interfacial layer for both the reference and annealed copper substrates. The thickness of the η -Cu₆Sn₅ layer was found to be independent of the substrate grain size but increased as the misorientation angle and the residual strain in the substrate increased.

1 Introduction

In the electronics industry, soldering, especially reflow soldering, is a key process in the assembly of electronics devices [1–3]. Due to its functionality and low cost, Sn–Cu alloys are commonly used as lead-free solder in the electronic packaging field [4, 5]. Copper is the most widely used substrate in underbump metallization (UBM) and ball grid arrays (BGAs) [5, 6]. This is because it possesses satisfactory electrical conductivity, easily dissolves into a molten solder during soldering, and the solder-substrate reactions induce an intermetallic compound (IMC) layer to form. The formation of a thin, continuous and uniform IMC layer is desirable for a satisfactory metallurgical bond. However, excessive IMC growth undermines the reliability of solder joints [6–9] due to increased brittleness and higher electrical resistivity [1–3]. In addition, the crystal orientation also affects the formation and growth of the IMC. Cu₆Sn₅ and Cu₃Sn form on a substrate with a preferred orientation. The lower misfit directions between the IMC and substrate promote intermetallic formation and growth [10–12].

The extents of the interfacial reactions and the IMC growth depend on a variety of factors, e.g., chemical reactions, volume diffusion and grain boundary diffusion [13–15]. Thus, it is operationally feasible to manipulate the IMC's growth behavior through substrate-solder alloy diffusion since it is a function of the substrate grain size [16, 17]. A review of the literature also revealed various phenomena in the IMC's growth behavior that depend on the substrate grain size. Cao et al. and Lee et al. [16, 18] observed that the thickness of the IMC increased with the fine grain size due to the increased diffusion path of the grain boundary, which enhanced the atomic diffusion and the growth rate of the intermetallic phase. Since atomic diffusion through a grain boundary is much faster than through a lattice, it has also been reported that the IMC's growth was reduced by using larger copper grain sizes. This was because of the lower diffusion path of copper atoms along the shortened grain boundary [19, 20]. In contrast, Wang et al. reported that the thickness of the IMC increased as the grain size increased. This was due to the presence of larger substrate grains, which promoted the combination of the chemical reaction and diffusion mechanisms. As the grain boundary of the substrate decreased, the atomic diffusion along the grain boundary also decreased. Thus, the diffusion became slower, thereby resulting in a transition from a diffusion mechanism to a chemical reaction mechanism [20]. The larger substrate grains accelerate the chemical reaction due to the dissolution

✉ Kannachai Kanlayasiri
kkkannac@kmitl.ac.th

¹ Department of Industrial Engineering, Faculty of Engineering, King Mongkut's Institute of Technology Ladkrabang, Bangkok 10520, Thailand

of copper atoms from the substrate into the solder. Hence, an increasing grain size would accelerate a chemical reaction at the interface, thereby resulting in a thicker IMC layer [21].

It has also been reported that the wetting of molten solder on micrometer-grain copper substrate outperformed that on nanocrystalline-grain substrate because due to the grain boundary, more adsorption of impurities takes place, thereby resulting in the reduction of the surface free energy [22]. Moreover, the grain boundary angle plays a crucial role in the stability of the liquid because a higher angle grain boundary (HAGB) with higher energy is more conducive to liquid wetting. A HAGB remains wetted by the liquid at a lower temperature compared to low-angle grain boundaries (LAGBs) [23–27].

This research aims at explaining the effects of the annealed copper substrate on the wettability of Sn–3.0Cu lead-free solder and on the growth of the intermetallic compound. The copper substrate was annealed at 300 °C, 600 °C and 900 °C for 1 h. Then, the electron backscatter diffraction (EBSD) technique was used to ascertain the grain orientation and the residual strain of the copper substrates.

2 Materials and procedure

2.1 Materials and sample preparation

The substrate that was used in this research was pure copper (99.99%) according to the JIS H3100 standard. The original copper substrate was manufactured via the rolled and half-hard tempering process. The substrate had a thickness of 1.5 mm and was cut into 20 × 10 mm rectangles, which were annealed at 300 °C, 600 °C and 900 °C for 1 h to vary the grain size. After annealing, the copper was polished with #1000 abrasive paper to remove the oxidized surface layer. The copper surface was cleaned in an HCl solution, cleaned in ethanol and air-dried. The surface roughness was evaluated by a surface roughness tester (Mahr, MarSurf PS1) with a cut-off length and scan length of 0.80 and 5.60 mm, respectively. The arithmetic mean roughness (R_a) of the original substrate and the substrate annealed at 300 °C, 600 °C, and 900 °C was approximately $0.058 \pm 4.5 \times 10^{-6}$ μm, $0.053 \pm 2.0 \times 10^{-6}$ μm, $0.065 \pm 8.0 \times 10^{-6}$ μm and $0.064 \pm 32 \times 10^{-6}$ μm, respectively. No significant difference between the surface roughness values was observed.

Sn–3.0Cu (in wt%) commercial lead-free solder from Ultracore Co., Ltd., which is a high-temperature lead-free solder within the alloy family, was used in this work. The weight percentage of the solder was confirmed using an optical emission spectrometer (ALR 3460 Thermo). The solidus and liquidus temperatures of the solder are 227 °C and 309 °C, respectively. Prior to soldering, the solder bar was cast into cylindrical solder rods of 6.5×1.24 mm in diameter

and thickness, which were 0.041 cm^3 in volume, according to the JIS Z3198-3: 2003 standard.

Reflow soldering was subsequently conducted at 350 °C using a hot plate. The flux droplets that were applied to the copper substrate were Ultracore flux, RC-15SH RMA (15%). The soldering time varied among 20, 40, 60 and 120 s.

2.2 Spreading and contact angle measurements

After soldering, the shape of the liquid solder spreading over the solid substrate was determined by a 3D scanner (GOM, ATOS Core 300). The scanned images were analyzed using the GOM Inspect software to determine the contact angles according to the JIS Z3198-3: 2003 standard.

2.3 Microstructure and crystallographic investigation

The substrate samples were ion milled using a HITACHI, IM 4000 PLUS. The grain microstructure was analyzed using an Olympus BX60M optical microscope and the grain size numbers (G) were determined using image-analysis software according to the ASTM E 1382 standard. The grain orientation was determined via electron backscatter diffraction (EBSD) using a HITACHI SU8230 field emission scanning electron microscope (FESEM) that was equipped with an OXFORD EBSD detector. The crystallographic texture of the substrate grains (the grain distribution) was determined based on pole figures (PFs), the grain orientation spread (GOS), misorientation angles (MOS) and the kernel average misorientation (KAM) using Emax Evolution 3.2.

The microstructure of the intermetallic compound (IMC) was determined using an OLYMPUS BX60M optical microscope and a JEOL JSM-5800LV scanning electron microscope (SEM). The IMC chemical composition was analyzed using an OXFORD INSTRUMENTS X-Max energy dispersive spectroscope (EDS). The IMC thickness (growth behavior) was examined based on 3500x SEM images using Image-Pro® Express and the IMC lattice structure was analyzed using a Bruker D8-Discover X-ray diffractometer (XRD).

3 Results and discussion

3.1 Microstructure of the copper substrates

The grain size numbers (G) of the copper substrates were determined via automatic image analysis with the intercept method, as illustrated in Fig. 1. A larger G value corresponds to a smaller grain size. The G value can be calculated via Eq. (1) [28]:

$$G = (6.643856 \log_{10} \bar{P}) - 3.288. \quad (1)$$

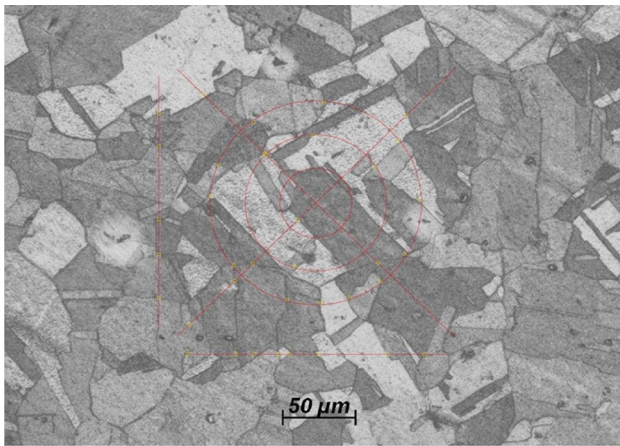


Fig. 1 Determination of G using the ASTM E112-10 intercept technique

where \bar{P} is the number of grain boundary intersections per unit length.

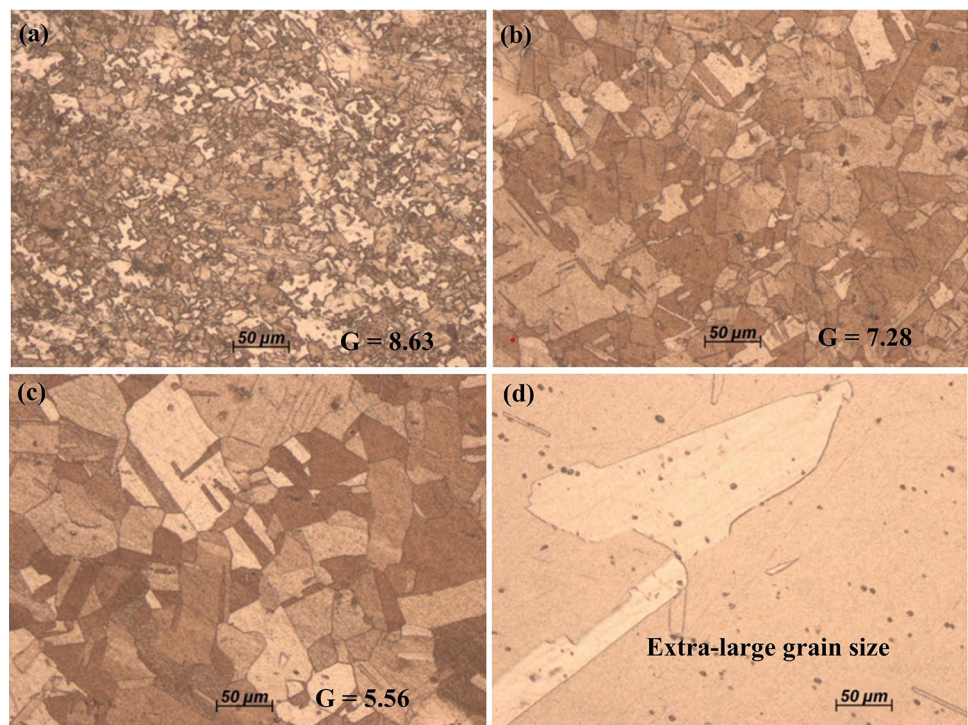
The microstructure images and corresponding G values of substrates are shown in Fig. 2. The microstructure of the reference Cu substrate (non-annealed) is presented in Fig. 2a, which exhibits a small grain size. Following the annealing treatment, the microstructure was modified as shown in Fig. 2b–d. The G values of the non-annealed and 300 °C- and 600 °C-annealed substrates were 8.63, 7.28 and 5.56, respectively. Hence, the increase of the annealing temperature led to an increased grain size. However,

the grain size of the 900 °C-annealed substrate exceeded the largest grain size under the ASTM standard [extralarge grain (ELG)].

The crystallographic textures (namely, the grain orientations) of the substrates in terms of multiples of the uniform distribution (MUDs) of PF for the {100}, {110} and {111} cubicle planes are shown in Fig. 3. The maximum MUDs of the non-annealed and 300 °C-, 600 °C- and 900 °C-annealed substrates were 11.03, 5.99, 8.92 and 42.48, respectively. The experimental results demonstrate that the higher annealing temperatures contributed to a larger angle preferred orientation, as evidenced by the higher MUD values. However, recrystallized grain may form in the subsequent stages of copper plate manufacturing processes [29]. The preferred orientation in the deformed substrate depends on the grain size and the annealing temperature. After thermal annealing, fine recrystallized grain was not detected; however, coarsening and growth of the grain were observed. Red regions in the spread of the nonuniform distribution were identified for all planes, thereby leading to the subsequent enhancement of the surface diffusion. Hence, the atoms could readily diffuse across the coarsening-grained substrate.

Interestingly, the orientation distribution became more uniform as the annealing temperature increased. The most red regions were observed with the copper substrate that was annealed at 900 °C, which was found to prefer the orientation of the {100} crystal planes, which are parallel to the X- and Y-axes. In these experiments, the X- and Y-axes

Fig. 2 Microstructure images of **a** the non-annealed and **b** 300 °C-, **c** 600 °C-, and **d** 900 °C-annealed substrates



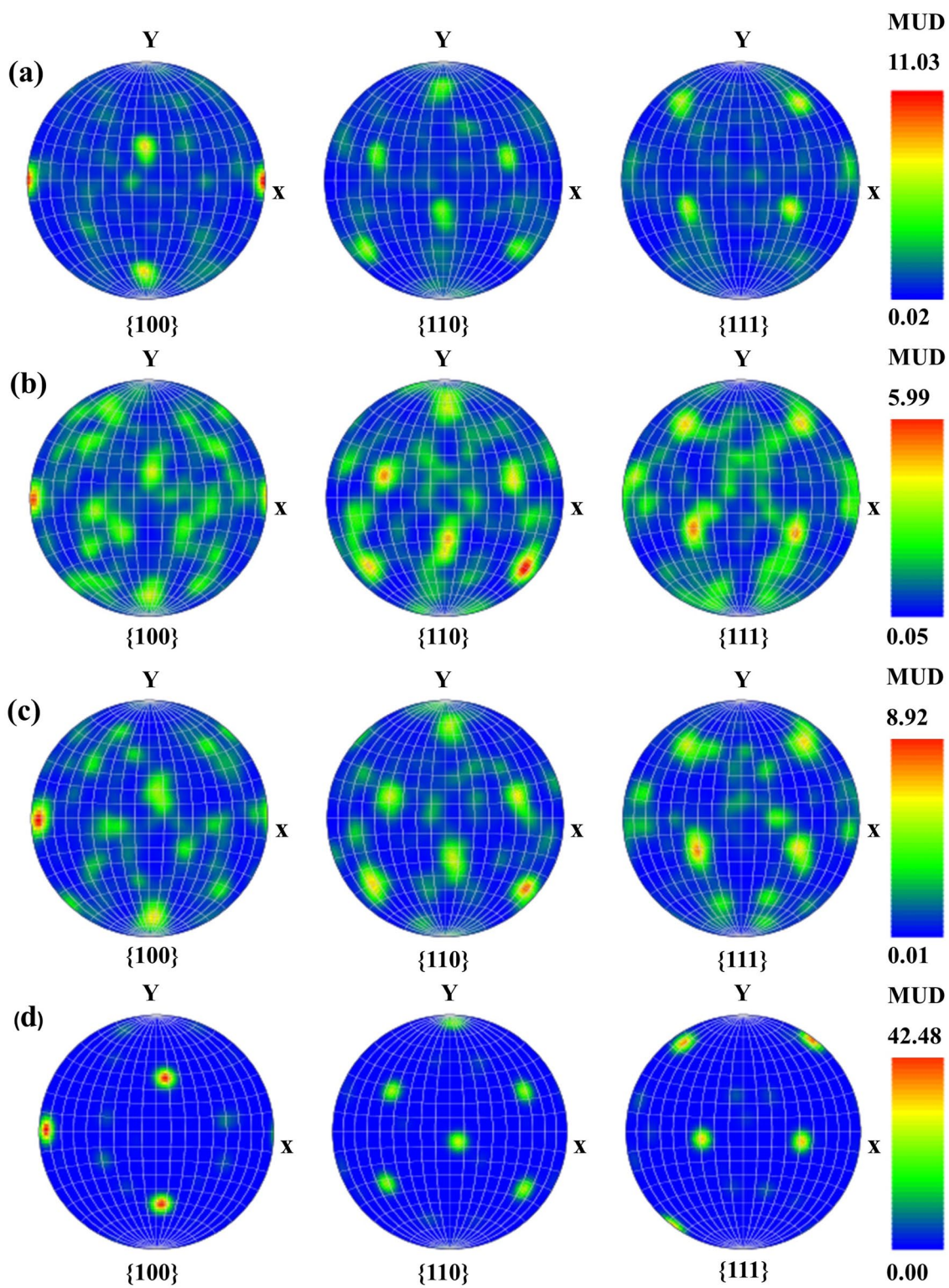


Fig. 3 Pole figures of **a** the non-annealed and **b** 300 °C-, **c** 600 °C-, and **d** 900 °C-annealed substrates

are defined by the rolling direction (RD) and the transverse direction (TD), respectively.

The grain orientation spread, or GOS, shows the average misorientation angle between each measured point (in a grain) and the average grain orientation. The GOS is used to distinguish between recrystallized and deformed grains. Figure 4a–d illustrate the GOSs of the non-annealed and 300 °C-, 600 °C- and 900 °C-annealed substrates, which have mean GOSs of 2.35°, 3.15°, 3.05° and 0.90°, respectively. A low GOS was realized under higher temperature annealing conditions, where stress relaxation occurred and large crystallized grains formed [30, 31]. In addition, a low GOS was attributable to a decrease in the grain dislocation density and deformation [32]. A lower GOS corresponds to a strain-free grain, while a higher value corresponds to retained deformation (strain) inside the grain [33]. The mean GOS value of the non-annealed substrate was lower than those of substrates with grain coarsening (300 °C and

600 °C). Intragranular misorientations reveal the presence of geometrically necessary dislocations and are indicative of stored energy. This can be interpreted as being almost fully recrystallized [34]. The higher energy dislocations are annihilated first; hence, the remaining dislocations correspond to low-energy configurations. Thus, the subsequent formation of grain structures is composed of low-angle grain boundaries. Therefore, high-temperature annealing outperformed low-temperature annealing in terms of the GOS value due to the lower average misorientation angle. Strong grain coarsening contributes to an increase in the average grain size and decreases in the grain boundary and grain misorientation [35].

However, the grain boundary angle in the microstructure affects the surface energy of the grain boundaries. The energy of a grain boundary increases with the grain boundary angle. Grain boundaries are divided into two main types: low-angle grain boundaries (LAGBs) and high-angle

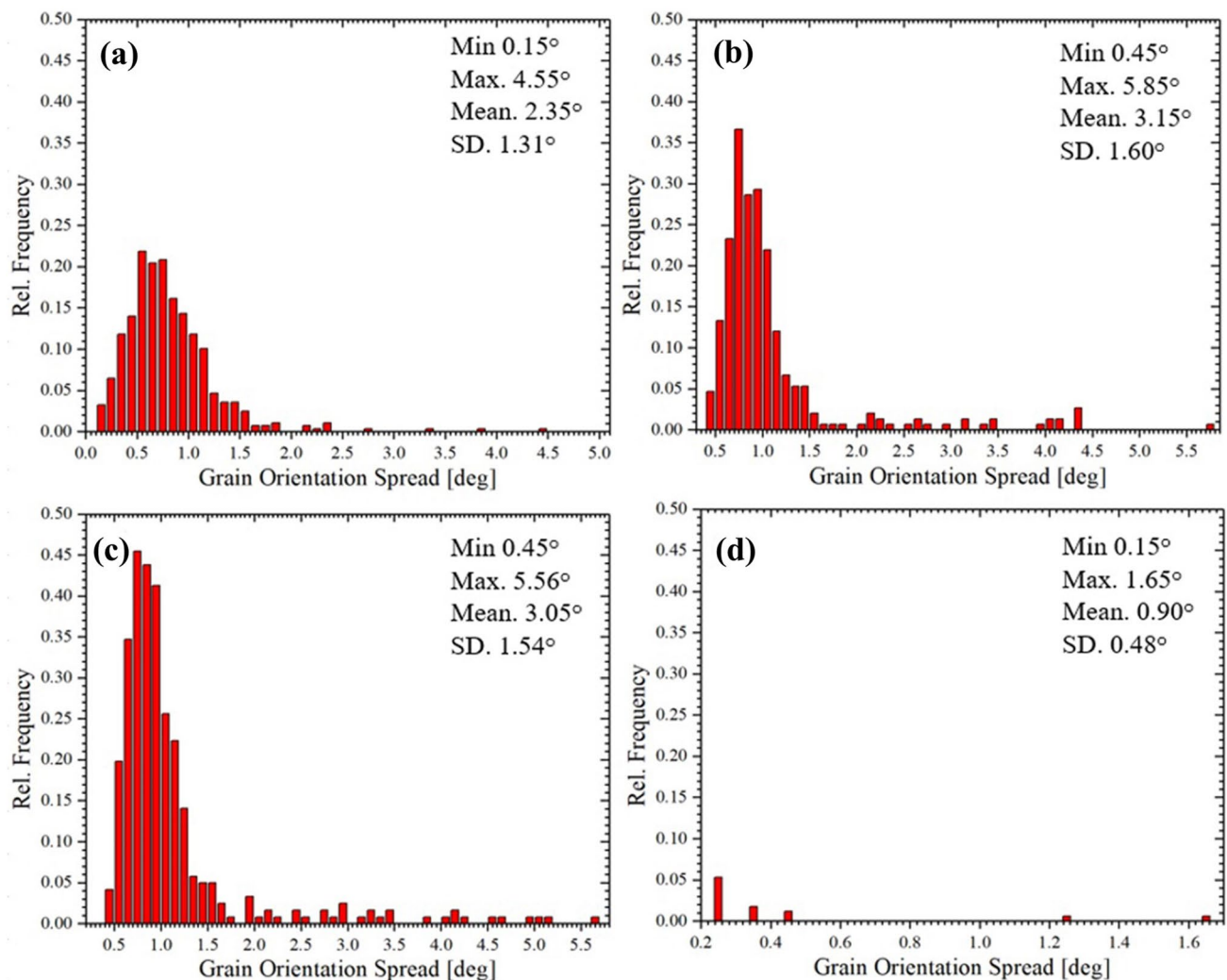


Fig. 4 Grain orientation spreads of the substrates: **a** the non-annealed and **b** 300 °C-, **c** 600 °C-, and **d** 900 °C-annealed substrates

grain boundaries (HAGBs). If the misorientation angle (MOS) between the grains exceeds 10° – 15° , the resultant grain boundaries are called HAGBs. If the misorientation angle is less than 10° , they are called LAGBs [36]. Figure 5 illustrates the grain boundaries of the substrates. The color of each boundary is related to the MOS. Most LAGBs for which the MOS is below 10° are colored red. HAGB is indicated by green and blue colors. Green HAGB corresponds to an MOS range of 10° – 50° , while blue HAGB corresponds to an MOS that exceeds 50° .

Grain growth occurs in both annealed substrates (300°C and 600°C) with large HAGB. The highly misoriented grain (shown in blue) contributed to the high residual strain of the copper substrate, which is consistent with the results of Glushko et al. [35] in that the strain increased with the grain refinement of HAGB. However, annihilation of the HAGB was observed at a high annealing temperature (900°C). Grain boundary relaxation occurs with high annealing temperature and a decrease in the grain boundary.

The local strain distribution in each grain was evaluated in terms of the kernel average misorientation (KAM). The KAMs for the substrates are plotted in Fig. 6. Higher KAM volumes (shown in green) were observed under the 300°C

and 600°C conditions, which correspond to higher dislocation density and higher strain compared to the non-annealing condition. At 300°C and 600°C , the larger GOS values and HAGBs were associated with higher strain. Under the 900°C annealing condition, the KAM volume was low, which suggests low dislocation density and strain with the increase in temperature. However, within the non-annealed substrate, strains and dislocation densities were observed that are attributable to residual strain hardening. This hardening occurred during the half-hard tempering process, which is consistent with Ho et al. [30]. Takayama et al. [37] report that the strain energy was lower during the deformation of fine-grained structures, as it is difficult for structures of this type to store energy during the high-temperature deformation. Hence, the strain energy is controlled by the grain dislocation density and deformation. The influence of the GOS and the residual strain also decreased under the preferred orientation.

3.2 Spreading and contact angle

The extent of solder spreading was determined by the wetting behavior of the solidified solder on the substrate. During

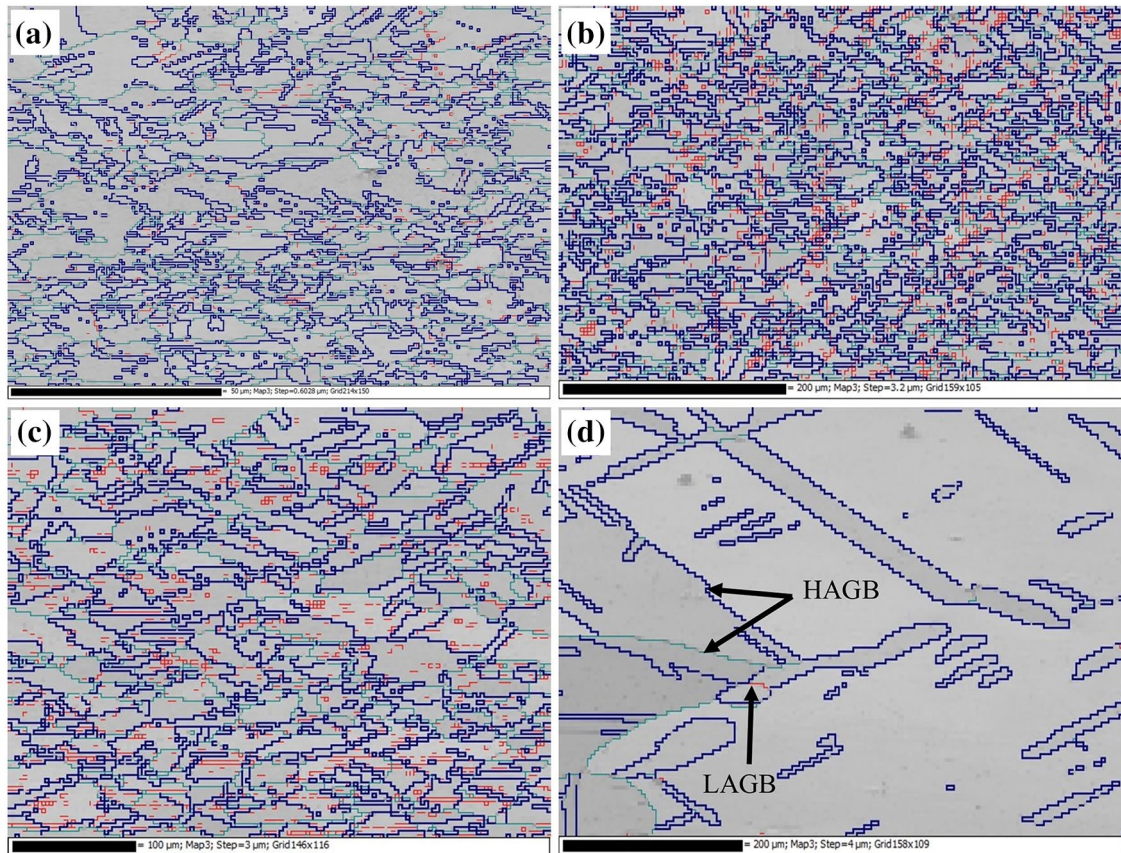


Fig. 5 Grain boundaries of the substrates: **a** the non-annealed and **b** 300°C -, **c** 600°C -, and **d** 900°C -annealed substrates

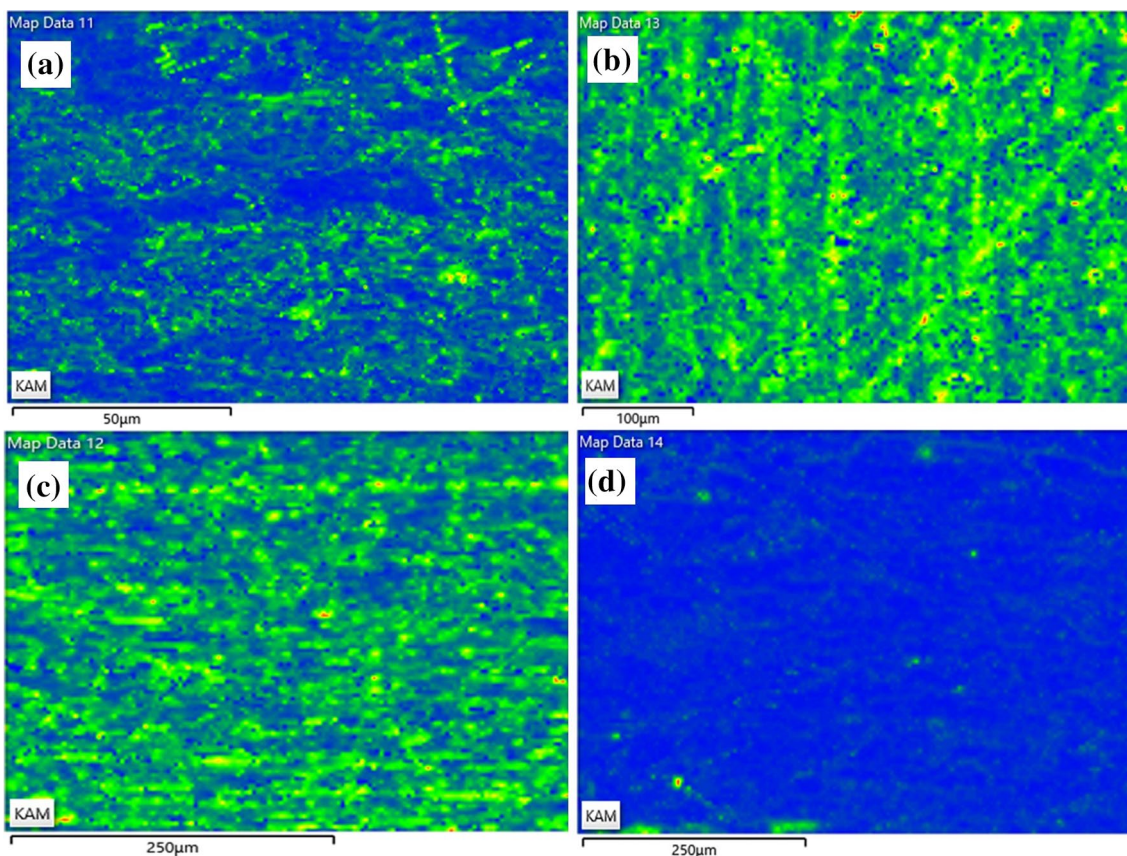


Fig. 6 Kernel average misorientation (KAM) of **a** the non-annealed and **b** 300 °C-, **c** 600 °C-, and **d** 900 °C-annealed substrates

soldering, the reduced surface energy caused the shape of the solder to change [38]. The increased contact area relative to the initial contact area corresponds to the wetting behavior of the solder, namely, the wettability is a function of the surface energy of the solid/liquid interface [39]. The solder wettability is determined by Young’s equation:

$$\gamma_{SF} = \gamma_{SL} + \gamma_{LF} \cos \theta_c \tag{2}$$

where γ_{SF} , γ_{LF} , and γ_{SL} are the surface tensions of the substrate/flux, liquid solder/flux, and substrate/liquid solder interfaces, respectively.

The 2D and 3D scan profiles of the postsoldering specimens (600 °C annealing) with a 120-s soldering time are illustrated in Fig. 7.

The wettability of the solder on the copper substrate is determined by the contact angle of the solder on the substrate. Figure 8 illustrates the contact angles (θ) for four soldering times (20, 40, 60, and 120 s) for G values of 8.63, 7.28, 5.56 and ELG for various substrates. For short soldering times (20–40 s), the initial wettability of the solder on small grains ($G = 8.63$) was less than on the large-grain substrate (annealing substrate) since the small grains have grain boundaries that can easily absorb impurities, namely,

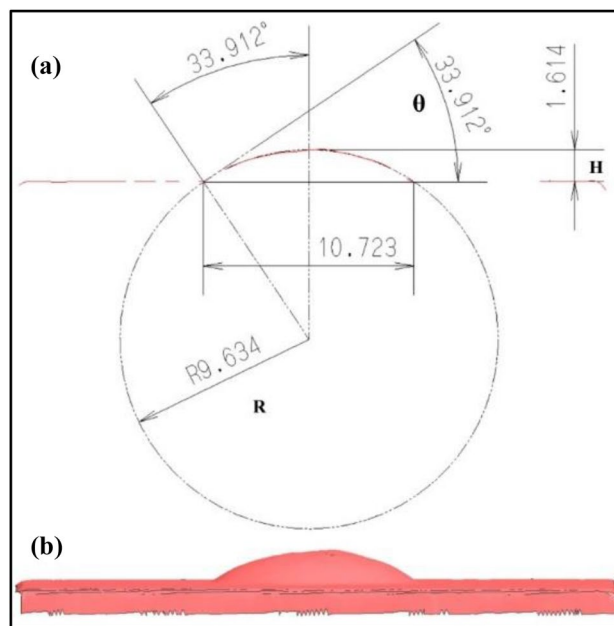


Fig. 7 Scan profiles of the postsoldering specimens (600 °C annealing) with a 120-s soldering time: **a** 2D and **b** 3D

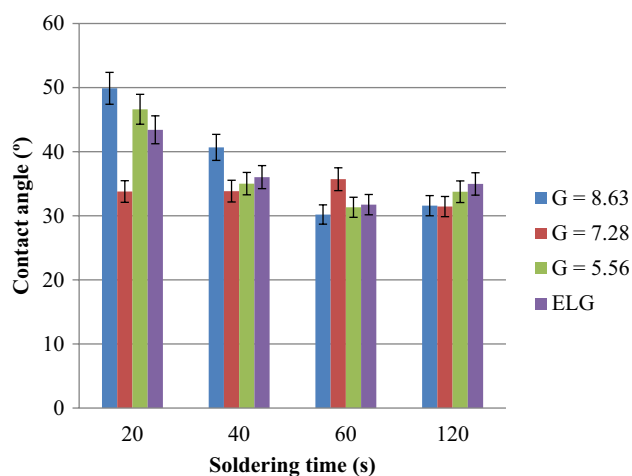


Fig. 8 Contact angles under four soldering times for G values of 8.63, 7.28, and 5.56 and ELG for the non-annealed and 300 °C-, 600 °C- and 900 °C-annealed substrates, respectively

residual oxygen and molecules. This leads to absorption and segregation on their surfaces/interfaces and residual oxygen results in decreased surface free energy [22]. Consequently, a short soldering time and the LAGB of the substrate provided a narrower spreading of non-annealed substrate than of annealed substrate. Hence, long soldering times (40, 60 and 120 s) resulted in negligible differences in contact angles, as the solder spreading had reached the equilibrium stage.

The relationship between the contact angle (θ) and the solder wettability is as follows: *excellent* wettability for $0^\circ < \theta < 30^\circ$; *satisfactory* wettability for $30^\circ < \theta < 40^\circ$; *fair* wettability for $40^\circ < \theta < 50^\circ$; *poor* wettability for $50^\circ < \theta < 70^\circ$; and *extremely poor* wettability for $\theta > 70^\circ$ [40, 41]. In this research, long soldering time contributed to decreased contact angles for all the substrate grain sizes. In addition, satisfactory solder wettability ($30^\circ < \theta < 40^\circ$) was realized under soldering times of 40, 60 and 120 s, with contact angles in the range of 30.19–40.67°. However, satisfactory solder

wettability was realized under long soldering times. During the first stage of contact between the liquid solder and a fresh substrate surface, the interface reaction rate is maximal, thereby leading to a rapid decrease in the contact angle. An exception to this is when incomplete melting of the solder affects the solid-phase content (mixture of the solid and liquid phases). An increase in the soldering time enables the solder to melt completely. Dissolution of the copper into the solder modifies the geometry at the triple line and, hence, the interfacial energies are modified. In addition, the contact angle decreases and gradually approaches equilibrium with the decrease in the reaction rate of the system. Thus, a long reaction time and a lower reaction rate lead to the assumption of the equilibrium contact angle. The substrate grain orientation has no effect on the solder wettability. When liquid metal droplets were present on various crystal orientations, they generated very similar wetting process results.

Table 1 presents the relationship between the grain size and the contact angle that was obtained in this study and comparable results from the literature [22, 42]. It is concluded that the findings of this study accord with the related literature, in which comparable time and grain size are reported. However, in this study, the contact angle of the wetting of the solder on the substrate was measured after soldering in the solid-state, while in previous work, the wetting was measured during heating. Hence, the contact angles of the solder may differ slightly between the two studies. Although the wetting was affected by surface roughness of the substrate [43], the surface roughness of copper substrate used in this study was not different. Therefore, the surface roughness did not significantly affect the wetting results.

4 Microstructure of the intermetallic compound

The intermetallic compound that formed between the solder and the substrate was Cu_6Sn_5 , as determined via EDS, with 51.43–59.30 at.% for Cu and 40.70–48.57 at.% for Sn; the

Table 1 Contact angles of solder for various substrate grain sizes

Soldering system	Substrate grain size	Initial contact angle	Stable contact angle	Soldering time/temperature	Ref.
Sn–3.0Cu/Cu	$18.14 \pm 1.15 \mu\text{m}$ (G = 8.63)	49.88°	30.19–31.57°	20–120 s 350 °C	This work
	$28.91 \pm 0.39 \mu\text{m}$ (G = 7.28)	33.78°	31.43–33.78°		
	$53.31 \pm 1.10 \mu\text{m}$ (G = 5.56)	46.61°	31.32–33.75°		
	ELG	43.15°	31.73–36.02°		
Sn3.5Ag0.7Cu/Cu	$30 \pm 10 \mu\text{m}$	55°	27–30°	0–25 s 228–284 °C	[42]
Sn3.5Ag0.7Cu/Ni	$30 \pm 10 \mu\text{m}$	70–75°	33–42°	0–1000 s 228–248 °C	

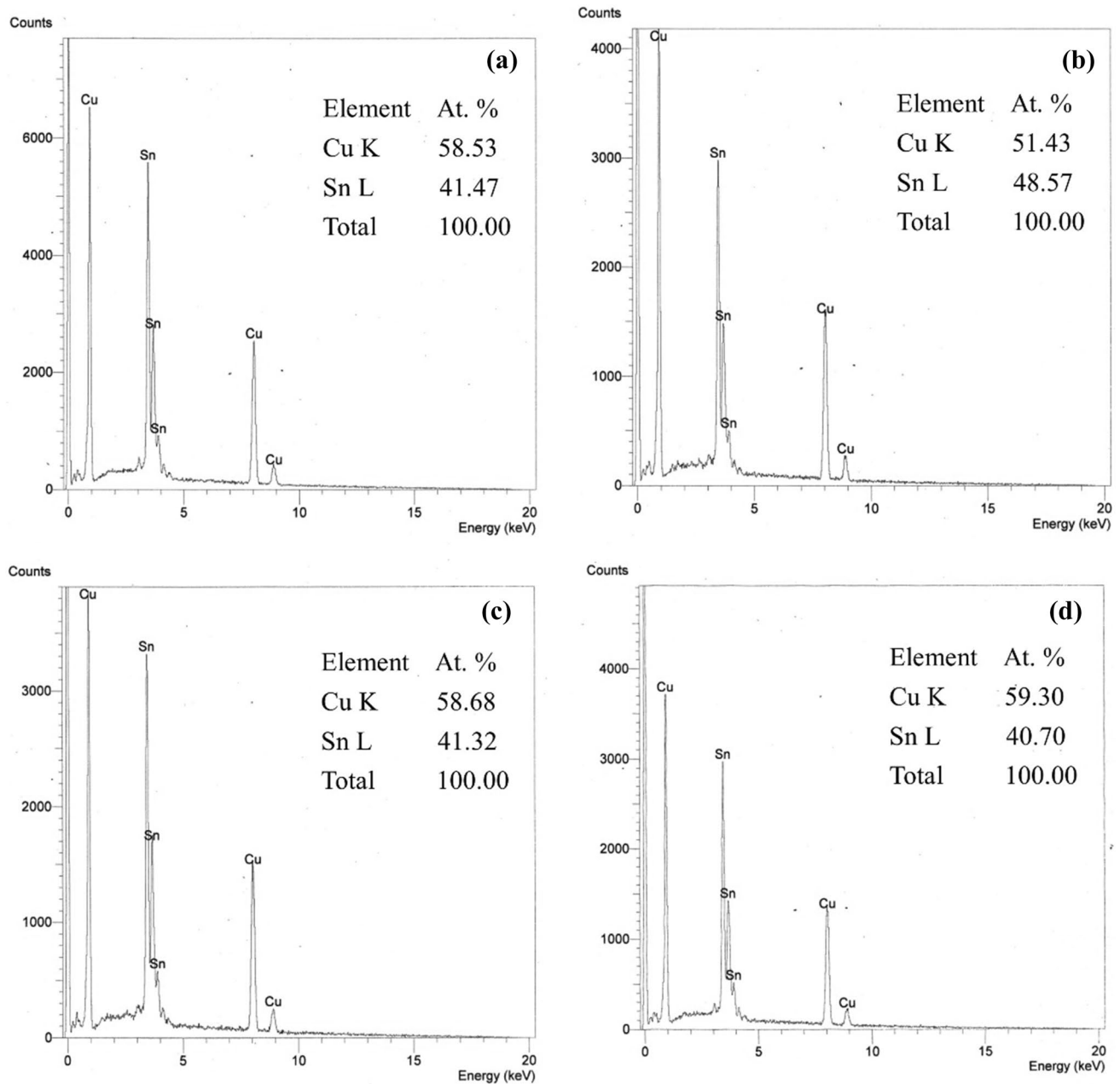


Fig. 9 EDS patterns of the soldered specimens: **a** the non-annealed and **b** 300 °C-, **c** 600 °C-, and **d** 900 °C-annealed substrates

EDS patterns are presented in Fig. 9. This chemical composition is consistent with the Cu_6Sn_5 phase according to the Sn–Cu phase diagram [44].

According to the XRD analysis, a single-phase hexagonal Cu_6Sn_5 intermetallic compound ($\eta\text{-Cu}_6\text{Sn}_5$) is present. Lattice parameters a , b and c of $\eta\text{-Cu}_6\text{Sn}_5$ were 0.4200, 0.4200 and 0.5090 nm. In addition, the $\eta\text{-Cu}_6\text{Sn}_5$ phase conforms to a B8_1 structure and a space group of $\text{P63}/\text{mmc}$, which is consistent with Refs. [45, 46]. A top view of the intermetallic phase after solder removal is shown in Fig. 10. The XRD patterns of the substrate specimens

under a 20-s soldering time are presented in Fig. 11. Nevertheless, neither $\eta'\text{-Cu}_6\text{Sn}_5$, which differs from $\eta\text{-Cu}_6\text{Sn}_5$ in terms of structure and is often detected at low temperatures, nor $\epsilon\text{-Cu}_3\text{Sn}$ was detected. However, it was reported that in the case of the Sn–Cu interface, the first phase ($\eta\text{-Cu}_6\text{Sn}_5$) was found at the solder/Cu interfaces and led to the formation of the $\epsilon\text{-Cu}_3\text{Sn}$ phase [23]. It is possible for $\epsilon\text{-Cu}_3\text{Sn}$ to form between the stable interfaces of $\eta\text{-Cu}_6\text{Sn}_5/\text{Cu}$. The formation of Cu_3Sn is more difficult: a longer soldering time is necessary for forming $\epsilon\text{-Cu}_3\text{Sn}$ [10, 47–49]. Furthermore, $\epsilon\text{-Cu}_3\text{Sn}$ was detected in a prior study at

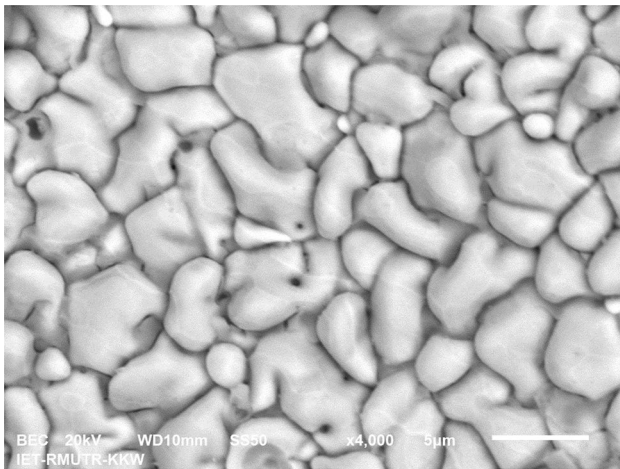


Fig. 10 Top-view SEM images of the η - Cu_6Sn_5 phase for determination via XRD

similar compositions and temperature ranges with longer reaction times (240 and 480 s) [49]. Hence, the η - Cu_6Sn_5 phase was not transformed into ε - Cu_3Sn under all soldering conditions. The η - Cu_6Sn_5 phase that was detected at the interface was of the scallop type.

SEM observation was conducted to study the intermetallic compounds (IMCs) at various soldering times and G

values, as shown in Fig. 12. Each IMC appears to be independent of the substrate grain size, since it depends on the orientation and the residual strain in the grain. The thickness of the IMC phase was found to increase as the misorientation angle and the residual strain in the substrate increase. Furthermore, the substrate grain size had no influence on the kinetics of IMC thickening. As a result of the difference between the G values (namely, between $G = 8.36$ and ELG), the thickness of the IMC differed slightly. The η - Cu_6Sn_5 phase forms on the (100) and (111) planes [10]. In this research, a stronger preferred orientation was detected at the (100) plane with a reduction in the formation of regions of nonuniform distribution on the (110) and (111) planes for the original and ELG substrates. Hence, the lower strain and diffusion with the preferred orientation of the substrate reduces the growth of the IMC.

The IMC growth (thickness) under various soldering times and grain sizes is plotted in Fig. 13. The IMC thickness was positively correlated with the soldering time and for the annealed substrate specimens, it was inversely correlated to the grain size. By comparison, the IMC growth of the annealed substrates was higher than that of the non-annealed substrate. This was due to deformed grains causing differences in the residual strain.

Regarding the trends that were observed in the IMC thickness in this work, it was found that the thickness of the IMC

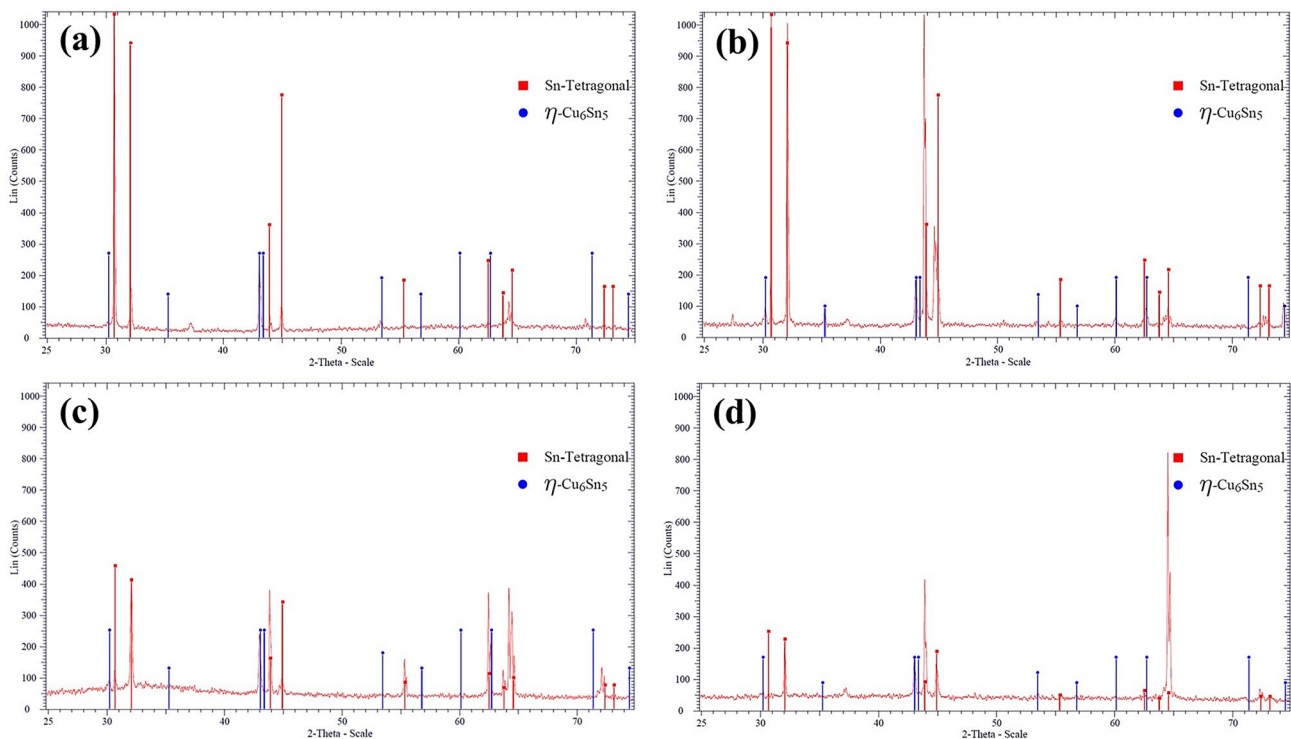


Fig. 11 XRD patterns of the soldered specimens under a 20-s soldering time: **a** the non-annealed and **b** 300 °C-, **c** 600 °C-, and **d** 900 °C-annealed substrates

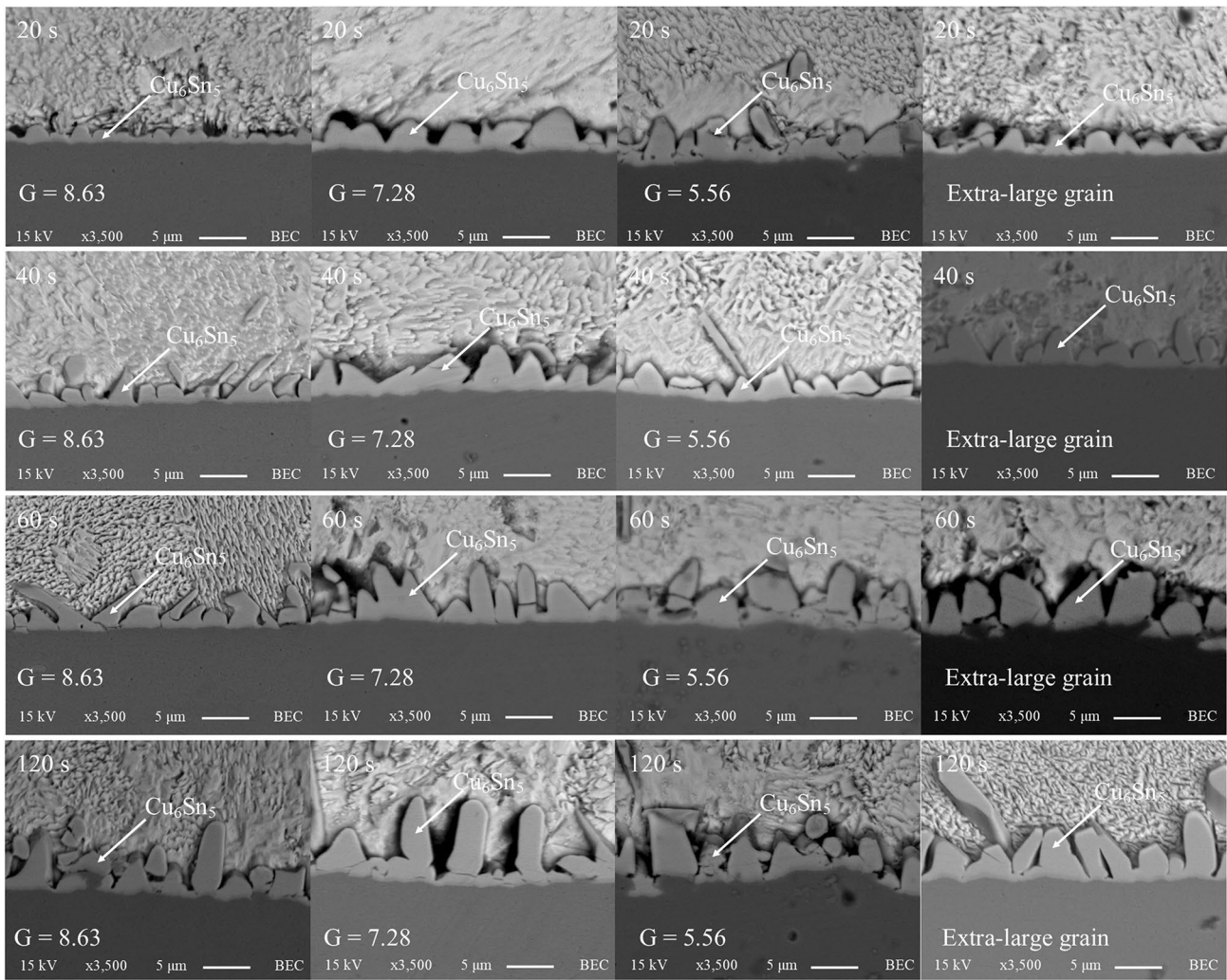


Fig. 12 SEM images of the intermetallic compound (Cu_6Sn_5) for four soldering times of 20, 40, 60 and 120 s and G values of 8.63, 7.28, 5.56 and ELG

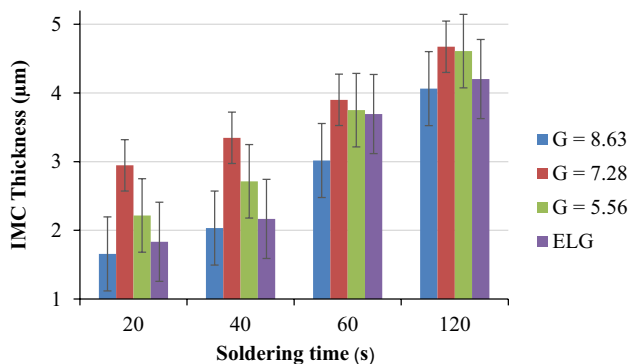


Fig. 13 IMC growth (thickness) under variable soldering time and grain size conditions

was independent of the substrate grain size. However, the thickness of the IMC of the original substrate was lower than those of the other substrates. This was because the diffusion of the copper atoms decreased as the residual strain decreased. Thus, the substrate grain size did not affect the kinetics of the IMC thickness. Substrates with high MOS and high residual strain have high energy. As the copper atoms are in an unstable high-energy state, they can easily change positions, thereby leading to improved diffusivity. The thicknesses of the intermetallic compounds increased as the diffusivity of the atom increased [50]. This suggested that the thickness of Cu_6Sn_5 was independent of the substrate grain size, whereas the IMC depended on the MOS and the strain within the substrate. According to the literature [19–21], various phenomena of the IMC's growth behavior as a function of the substrate grain size have been observed.

However, it was demonstrated in this study that the thickness of the IMC does not necessarily increase with the fine grain size due to the diffusion path of the grain boundary. Due to effect of the residual strain on the grain boundary diffusion, the increase in the residual strain led to increased diffusion.

Larger MOS values are associated with higher diffusivity. In addition, the IMC thickness increased with the MOS and the residual strain. This is consistent with the results of Kim et al. [51], who demonstrated that a larger MOS is associated with larger diffusivity and that atomic diffusion is independent of the grain size. The intermetallic thickness is a function of the misorientation angle and the residual strain of the annealed substrate grain. However, an insignificant change in the substrate grain size was recorded as the soldering time increased [49].

In summary, the research results that are presented here demonstrate that the substrate grain size has no direct influence on the formation and growth of the intermetallic compound (IMC), while the MOS and the residual strain are correlated to the IMC thickness. Thus, the MOS, dislocation density and strain of the substrate are important for controlling the thickness of IMC during the soldering process.

5 Conclusions

This research has examined the effects of various copper substrate grain sizes on the contact angle and the spreading of Sn–3.0Cu lead-free solder and on intermetallic compound (IMC) formation and growth. The substrate grain sizes were varied by annealing at 300 °C, 600 °C and 900 °C for 1 h. Four copper substrates were used: a non-annealed reference and 300 °C-, 600 °C- and 900 °C-annealed specimens. Reflow soldering using Sn–3.0Cu lead-free solder was subsequently conducted with the non-annealed and annealed copper substrates at 350 °C under soldering times of 20, 40, 60 and 120 s. The experimental results demonstrated that the substrate grain orientation and strain had no effect on the solder wettability. In addition, the solder spreading exhibited a nonuniform pattern due to a decrease in the interfacial total free energy. Satisfactory solder wettability ($30^\circ < \theta < 40^\circ$) was realized under soldering times of 40, 60 and 120 s for which contact angles in the range of 30.19°–40.67° were observed. The single-phase hexagonal Cu₆Sn₅ intermetallic compound was present in the interfacial layer between the lead-free solder and the non-annealed and annealed copper substrates. Furthermore, the IMC growth behavior was positively correlated to the soldering time, while the

IMC growth was directly correlated to the MOS and the residual strain.

Acknowledgments The authors would like to express sincere gratitude to Faculty of Engineering of King Mongkut's Institute of Technology Ladkrabang (KMITL) for financial support.

Data availability The raw/processed data that are required for reproducing these findings cannot be shared at this time as the data also constitute part of an ongoing study.

References

1. F.Y. Ouyang, Y.P. Su, J. Alloy. Compd. **655**, 155 (2016)
2. Q.K. Zhang, W.M. Long, Z.F. Zhang, J. Alloy. Compd. **646**, 405 (2015)
3. H. Nishikawa, N. Iwata, J. Mater. Process. Technol. **215**, 6 (2015)
4. J. Koo, J. Chang, Y.W. Lee, S.J. Hong, K.-S. Kim, H.M. Lee, J. Alloy. Compd. **608**, 126 (2014)
5. M.J. Rizvi, C. Bailey, Y.C. Chan, M.N. Islam, H. Lu, J. Alloy. Compd. **438**, 122 (2007)
6. A. Sharif, Y.C. Chan, Mater. Sci. Eng., B **106**, 126 (2004)
7. T. Laurila, V. Vuorinen, J.K. Kivilahti, Mater. Sci. Eng. **49**, 1 (2005)
8. G.K. Sujana, A.S.M.A. Haseeb, A.B.M. Afifi, Mater. Charact. **97**, 199 (2014)
9. P.J. Shang, Z.Q. Liu, D.X. Li, J.K. Shang, J. Electron. Mater. **38**, 2579 (2009)
10. R. Zhang, Y. Tian, B. Liu, C. Hang, in *2013 14th International Conference On Electronic Packaging Technology (ICEPT)* (IEEE, 2013), pp. 1276–1279
11. J.O. Suh, K.N. Tu, J. Appl. Phys. **102**, 1 (2007)
12. K.N. Tu, *Solder Joint Technology* (Springer, New York, 2007)
13. O.M. Abdelhadi, L. Ladani, J. Alloy. Compd. **537**, 87 (2012)
14. J. Shen, Y.C. Chan, S.Y. Liu, Acta Mater. **57**, 5196 (2009)
15. M. Schaefer, R.A. Fournelle, J. Liang, J. Electron. Mater. **27**, 1167 (1998)
16. K. Cao, K. Tan, C. Lai, L. Zhang, in *2009 International Conference on Electronic Packaging Technology & High Density Packaging* (IEEE, 2009), pp. 819–823
17. R. Abbaschian, R.E. Reed-Hill, *Physical Metallurgy Principles* (Cengage Learning, Boston, 2008)
18. P.T. Lee, Y.S. Wu, P.C. Lin, C.C. Chen, W.Z. Hsieh, C.E. Ho, Surf. Coat. Technol. **320**, 559 (2017)
19. Y.J. Li, C. Chen, in *Microsystems, Packaging, Assembly and Circuits Technology Conference (IMPACT), 2016 11th International* (IEEE, 2016), pp. 42–44
20. J.M. Wang, K.J. Wang, J.G. Duh, J. Electron. Mater. **40**, 1549 (2011)
21. M.L. Huang, F. Yang, Sci. Rep. **4**, 7117 (2014). <https://doi.org/10.1038/srep07117>
22. P. Shen, Z. Yin, J. Yang, J. Sun, Z. Jiang, Q. Jiang, Surf. Interface Anal. **42**, 1681 (2010)
23. B.J. Lee, N.M. Hwang, H.M. Lee, Acta Mater. **45**, 1867 (1997)
24. E. Chauvet, P. Kontis, E.A. Jägle, B. Gault, D. Raabe, C. Tassin, J.J. Blandin, R. Dendievel, B. Vayre, S. Abed, Acta Mater. **142**, 82 (2018)
25. B.B. Straumal, B.S. Bokshstein, A.B. Straumal, A.L. Petelin, JETP Lett. **88**, 537 (2008)

26. A.S. Gornakova, B.B. Straumal, S. Tsurekawa, L.S. Chang, A.N. Nekrasov, *Rev. Adv. Mater. Sci.* **21**, 18 (2009)
27. E. Rabkin, I. Snapiro, *Acta Mater.* **48**, 4463 (2000)
28. ASTM, in *ASTM International E 112-12* (2012), pp. 1–27
29. L.A.I. Kestens, H. Pirgazi, *Mater. Sci. Technol.* **32**, 1303 (2016)
30. C.E. Ho, C.C. Chen, M.K. Lu, Y.W. Lee, Y.S. Wu, *Surf. Coat. Technol.* **303**, 86 (2016)
31. M.R. Akbarpour, M. Farvizi, H.S. Kim, *Mater. Des.* **119**, 311 (2017)
32. D.P. Field, L.T. Bradford, M.M. Nowell, T.M. Lillo, *Acta Mater.* **55**, 4233 (2007)
33. D. Yadav, R. Bauri, *Mater. Sci. Technol.* **31**, 494 (2015)
34. N. Bozzolo, A. Agnoli, N. Souai, M. Bernacki, R.E. Logé, *Mater. Sci. Forum* **753**, 321 (2013)
35. O. Glushko, M.J. Cordill, *Scr. Mater.* **130**, 42 (2017)
36. Z.D. Jastrzebski, *The Nature of Properties of Engineering Materials*, 2nd edn. (Wiley, New York, 1987)
37. Y. Takayama, J.A. Szpunar, H. Kato, *Mater. Sci. Forum* **495–497**, 1049 (2009)
38. C.M.L. Wu, D.Q. Yu, C.M.T. Law, L. Wang, *Mater. Sci. Eng.* **44**, 1 (2004)
39. Satyanarayan, K.N. Prabhu, *Adv. Colloid Interface Sci.* **166**, 87 (2011)
40. L. Zang, Z. Yuan, H. Xu, B. Xu, *Appl. Surf. Sci.* **257**, 4877 (2011)
41. A. Wedi, D. Baither, G. Schmitz, *Scr. Mater.* **64**, 689 (2011)
42. J. Yang, P. Shen, Z. Yin, J. Sun, Q. Jiang, *Mater. Lett.* **64**, 2454 (2010)
43. Satyanarayan, K.N. Prabhu, in *National Conference on Challenges in Research & Technology in the Coming Decades (CRT 2013)* (Institution of Engineering and Technology, 2013), pp. 3.31–3.31
44. H. Okamoto, M.E. Schlesinger, E.M. Mueller, *ASM Handbook Volume 3: Alloy Phase Diagrams* (ASM International, 2016)
45. H.W. Lin, C.L. Lu, C.M. Liu, C. Chen, D. Chen, J.C. Kuo, K.N. Tu, *Acta Mater.* **61**, 4910 (2013)
46. H. Chi Won, J.G. Lee, S. Katsuaki, M. Hiroto, J. Electron. Mater. **32**, 52 (2003)
47. N. Mookam, P. Tunthawiroon, K. Kanlayasiri, in *IOP Conference Series: Materials Science and Engineering* (2018)
48. S.R. A. Idris, N. Farihan, H. Kahar, in *MATEC Web of Conferences*, vol. 74 (2016), pp. 1–3
49. N. Mookam, K. Kanlayasiri, in *MATEC Web of Conferences 192,(2018) ICEAST 2018* (2018), pp. 1–4
50. T. An, F. Qin, *Microelectron. Reliab.* **54**, 932 (2014)
51. K.S. Kim, J.H. Kim, S.W. Han, *Mater. Lett.* **62**, 1867 (2008)

Publisher's Note Springer Nature remains neutral with regard to jurisdictional claims in published maps and institutional affiliations.